Small-scale anisotropic intermittency in magnetohydrodynamic turbulence at low magnetic Reynolds numbers

Naoya Okamoto, Katsunori Yoshimatsu, Kai Schneider, Marie Farge

Small-scale anisotropic intermittency in magnetohydrodynamic turbulence at low magnetic Reynolds numbers

Naoya Okamoto,[1] Katsunori Yoshimatsu,[2] Kai Schneider,[3] and Marie Farge[4]
[1]*Center for Computational Science, Nagoya University, Nagoya, 464–8603, Japan*
[2]*Department of Computational Science and Engineering, Nagoya University, Nagoya, 464–8603, Japan*
[3]*M2P2–CNRS and CMI, Aix-Marseille Université, 38 rue F. Joliot-Curie, 13451 Marseille Cedex 20, France*
[4]*LMD–IPSL–CNRS, Ecole Normale Supérieure, 24 rue Lhomond, 75231 Paris Cedex 05, France*
(Received 20 December 2013; published 14 March 2014)

Small-scale anisotropic intermittency is examined in three-dimensional incompressible magnetohydrodynamic turbulence subjected to a uniformly imposed magnetic field. Orthonormal wavelet analyses are applied to direct numerical simulation data at moderate Reynolds number and for different interaction parameters. The magnetic Reynolds number is sufficiently low such that the quasistatic approximation can be applied. Scale-dependent statistical measures are introduced to quantify anisotropy in terms of the flow components, either parallel or perpendicular to the imposed magnetic field, and in terms of the different directions. Moreover, the flow intermittency is shown to increase with increasing values of the interaction parameter, which is reflected in strongly growing flatness values when the scale decreases. The scale-dependent anisotropy of energy is found to be independent of scale for all considered values of the interaction parameter. The strength of the imposed magnetic field does amplify the anisotropy of the flow.

DOI: 10.1103/PhysRevE.89.033013 PACS number(s): 47.27.Ak, 47.65.Cb, 47.27.E−, 47.27.Gs

I. INTRODUCTION

Turbulence of electrically conducting fluids subjected to external magnetic field at low magnetic Reynolds number is encountered in geophysical flows, e.g., the geodynamo, and in numerous machines, e.g., electromagnetic casting of melted metals and cooling blankets of nuclear reactors [1]. The imposed magnetic field can be assumed to be uniform for small-scale turbulence. Mathematical modeling of the Lorentz force leads to the so-called quasistatic (QS) approximation of magnetohydrodynamic (MHD) turbulence, therefore called QS MHD turbulence; see, e.g., [2]. The intensity of the Lorentz force, due to the imposed magnetic field, compared to flow inertia is characterized by the magnetic interaction parameter, sometimes called the Stuart number, while the turbulence intensity is quantified by the kinetic Reynolds number. The Lorentz force is anisotropic and suppresses turbulence [3].

Experiments with liquid-metal flows present difficulties for measuring and visualizing the relevant fields, owing to the opacity of the liquid metals and their corrosion. Therefore, direct numerical simulation (DNS) is an essential tool to obtain statistics on the turbulent flows and flow structures encountered in those experiments. In the current work, homogeneous flows are considered which allow for periodic boundary conditions. Hence, efficient Fourier pseudospectral methods can be used for solving the underlying equations by means of DNS.

Since the pioneering work of Schumann [4], DNS studies of three-dimensional (3D) QS MHD turbulence have been carried out for canonical turbulent flows, e.g., homogeneous turbulence. It was shown that vorticity structures have the tendency to be aligned with the direction of the imposed magnetic field [5]. Scale-by-scale flow anisotropy was quantified by the Fourier representation of the two-point velocity correlations. It was observed that flow anisotropy is stronger as the interaction parameter increases, see, e.g., [4–7]. Two types of anisotropy measured by the use of the 3D energy spectra are persistent at small scales for turbulence, even at modest kinetic Reynolds numbers, and their scale dependence is weak [7]. In Ref. [6], one-dimensional (1D) spectra of each velocity component in the longitudinal direction showed that the component parallel to the imposed magnetic field is more attenuated at small scale than the components perpendicular to the magnetic field. Ishida and Kaneda [8] predicted the scale dependence and the angular dependence of the anisotropic velocity correlation spectrum in the inertial subrange, using the response of the equilibrium state to the external magnetic field. They showed that the predicted spectrum is in good agreement with their DNS results. In long-time simulations of decaying QS MHD turbulence, one observes the transition from 3D to 2D and three-component turbulence predicted by [9], which results from the Joule dissipation and generation of polarization anisotropy due to nonlinear interaction [10]. Due to the decay of the kinetic energy, the level of turbulence is strongly reduced. Readers interested in DNS of wall-bounded turbulent QS MHD flows may refer to a review article [11].

Fourier techniques yield insight into wave-number-dependent, i.e., scale-dependent second-order velocity moments of turbulent flows in different directions, as mentioned above. However, their spatial fluctuations at different scales cannot be quantified owing to the global character of the Fourier basis functions. Hence, one is then not able to quantify the anisotropy of the spatial fluctuations and the flow intermittency at each scale. Wavelets, being well-localized functions in space, scale, and direction, yield a nonredundant orthogonal representation of flows, allowing us to quantify both anisotropy and intermittency. Bos *et al.* [12] introduced directional scale-dependent wavelet statistics, for example, flatness factors, which yield intermittency measures of anisotropic turbulence. Wavelet techniques have been applied in hydrodynamic [12–16], MHD [17], and solar-wind turbulence for analysis [18–20], for modeling [21,22], and for computing turbulent flows [23,24].

In this paper, we examine the anisotropy of spatial fluctuations and of intermittency for QS MHD turbulence of small scales. Emphasis is put on scale dependence and on the influence of the magnetic field strength. We thus propose to extend the wavelet-based statistics developed in Ref. [12] and introduce scale-dependent statistical measures in order to quantify the anisotropy of the spatial fluctuations of the different flow components, either parallel or perpendicular to the imposed magnetic field, and to relate these measures to the flow intermittency. Anisotropy in different flow directions, either longitudinal or transverse, can be quantified too.

We perform DNS of 3D QS MHD turbulence in a periodic box, using solenoidal forcing imposed only on the large-scale flow. The motivation for applying such a forcing is to obtain statistically quasistationary small-scale turbulence while keeping the kinetic Reynolds number as high as possible.

The remainder of the paper is organized as follows. First, we briefly recall the basic equations of QS MHD turbulence in Sec. II and describe the numerical approach used to solve them. Then the wavelet methodology and the statistical measures based on it are introduced in Sec. III. Numerical results are presented in Sec. IV. Finally, Sec. V draws some conclusions and gives perspectives for future work.

II. BASIC EQUATIONS AND DIRECT NUMERICAL SIMULATION

We consider the 3D turbulent motions of an incompressible electrically conducting fluid in a periodic cube with side length 2π, subjected to a uniformly imposed magnetic field $\boldsymbol{B}_0$. Statistically the motions yield axisymmetry and reflectional symmetry. Their magnetic Reynolds numbers are assumed to be sufficiently small such that the QS MHD approximation can be applied. We use Cartesian coordinates and set $\boldsymbol{B}_0$ to $(0,0,B_0)$ without loss of generality. The velocity field $\boldsymbol{u}(\boldsymbol{x},t)$ obeys

$$\frac{\partial \boldsymbol{u}}{\partial t} + (\boldsymbol{u}\cdot\nabla)\boldsymbol{u} = -\frac{1}{\rho}\nabla p + \nu\nabla^2\boldsymbol{u} - \frac{\sigma B_0^2}{\rho}\Delta^{-1}\frac{\partial^2 \boldsymbol{u}}{\partial x_3^2} + \boldsymbol{f}, \tag{1}$$

$$\nabla\cdot\boldsymbol{u} = 0, \tag{2}$$

where $\boldsymbol{x} = (x_1,x_2,x_3)$, $\nabla = (\partial/\partial x_1, \partial/\partial x_2, \partial/\partial x_3)$, Δ^{-1} represents the inverse Laplace operator, t the time, $\boldsymbol{f}(\boldsymbol{x},t)$ an external solenoidal forcing, $p(\boldsymbol{x},t)$ the modified pressure including the magnetic pressure, ν the kinematic viscosity, ρ the density, and σ the electrical conductivity. In Eqs. (1) and (2), and hereafter, we omit the arguments $\boldsymbol{x}$ and t, if not otherwise stated.

Equations (1) and (2) are solved by DNS at resolution 512^3, using a dealiased Fourier pseudospectral method with a fourth-order Runge-Kutta method for time marching. Aliasing errors are removed by a phase-shift method and a spherical spectral cutoff retaining only Fourier modes satisfying $k \leqslant k_{\max}$. Here, $k = |\boldsymbol{k}|$, where $\boldsymbol{k}$ is the wave vector, $k_{\max}$ is the maximum integer smaller than $2^{1/2}n/3$, and $n = 512$ is the number of grid points in one Cartesian direction. We impose the same type of forcing as introduced in Ref. [7]. To retain active large-scale three dimensionality, only the low wave-number range $k < 2.5$ is forced and the total kinetic energy is kept at a constant value of 0.5. The forcing is defined as

$$\widehat{\boldsymbol{f}}(\boldsymbol{k}) = \frac{\langle\epsilon_v\rangle + \langle\epsilon_m\rangle}{n_f|\widehat{\boldsymbol{u}}(\boldsymbol{k})|^2}\widehat{\boldsymbol{u}}(\boldsymbol{k}), \tag{3}$$

where $\widehat{\cdot}$ is the Fourier transformation of $\cdot$, n_f is the number of Fourier modes subjected to the forcing, $\langle\epsilon_v\rangle$ is the mean kinetic energy dissipation rate per unit mass, and $\langle\epsilon_m\rangle$ is the Joule dissipation rate per unit mass. The kinematic viscosity is $\nu = 2.8\times10^{-4}$, and the time increment is 1.0×10^{-3}. Different values for the intensity of the uniform magnetic field B_0 are chosen such that the interaction parameters N are equal to 0, 1, and 2, respectively. The interaction parameter is defined by

$$N = \frac{\sigma B_0^2 L}{\rho u'}, \tag{4}$$

which characterizes the intensity B_0 relative to the flow nonlinearity. Here, $u' = (\langle|\boldsymbol{u}|^2\rangle/3)^{1/2}$, where $\langle\cdot\rangle$ denotes the spatial average of $\cdot$, and L is the initial integral length scale defined by $L = \pi/(2u'^2)\int_0^{k_{\max}} e(k)/k\,dk$, where $e(k)$ is the energy spectrum defined by $e(k) = \sum_{i=1}^3 e^{(i)}(k)$ with $e^{(i)}(k) = \sum_{k-1/2\leqslant|\boldsymbol{q}|<k+1/2}|\hat{u}^{(i)}(\boldsymbol{q})|^2/2$.

The DNS computations for $N = 0$, 1, and 2, respectively called RunN0, RunN1, and RunN2, are performed up to the final time instants: $(t-t_0)/T \simeq 1.14$ for RunN0, and $(t-t_0)/T \simeq 6.31$ for RunN1 and RunN2, where T denotes the initial large-eddy turnover time defined by $T = u'/L$, and t_0 is the initial time. The flow in RunN0 can be considered as hydrodynamic turbulence. The resulting flows are statistically quasistationary at small scales in the sense that $\langle\epsilon_v\rangle$ and the component-wise anisotropic measure $c(k)$ only slightly change in time at small scales, where

$$c(k) = \frac{e^{(1)}(k) + e^{(2)}(k)}{2e^{(3)}(k)}. \tag{5}$$

Table I summarizes the statistics at the final time, the Taylor microscale Reynolds number R_λ, the Kolmogorov length scale η, $\langle\epsilon_v\rangle$, and $\langle\epsilon_m\rangle$, where $R_\lambda = u'\lambda/\nu$, $\lambda = (15\nu u'^2/\langle\epsilon_v\rangle)^{1/2}$, and $\eta = (\nu^3/\langle\epsilon_v\rangle)^{1/4}$. It is shown that R_λ increases with N, owing to the reduction of $\langle\epsilon_v\rangle$ with increasing N, as observed in Ref. [25] where a random solenoidal forcing was used. It can be noted that the results which will be presented in Sec. IV are confirmed to be robust, using the data from [25].

TABLE I. Statistics of the DNS computations for RunN0, RunN1, and RunN2 at the final time instant.

	N	R_λ	$k_{\max}\eta$	$\langle\epsilon_v\rangle$	$\langle\epsilon_m\rangle$
RunN0	0	226	1.02	10.2×10^{-2}	0
RunN1	1	359	1.29	4.03×10^{-2}	14.4×10^{-2}
RunN2	2	581	1.64	1.54×10^{-2}	20.8×10^{-2}

The field used to initialize the DNS computations is a quasistationary hydrodynamic turbulent flow at $R_\lambda = 235$, which was computed by a preceding DNS with the same parameters of RunN0. We consider only DNS data for $N = 0$, 1, and 2, because for larger N it would take much more time to reach a statistically quasistationary state. For example, the level of $c(k)$ at small scales decays in time for $N = 4$, and

reaching a statistically steady state takes 1.3 times longer than for RunN2.

III. METHODOLOGY

In the following, we give a brief summary of orthogonal wavelet analysis applied to the velocity field. The wavelet representation allows us to measure scale-dependent distributions of turbulent flows in different directions and also of the different flow components. For example, not only energy but also its spatial fluctuations can be quantified at different length scales and in different directions. Thus, longitudinal or transverse contributions can be distinguished, as well as contributions in the directions perpendicular or parallel to the imposed magnetic field. Therefore, statistical quantities based on the wavelet representation are introduced in order to examine scale-dependent anisotropy and the corresponding intermittency of low magnetic Reynolds number turbulence. Intermittency is defined here as a departure from Gaussianity, reflected by the fact that the flatness increases when scale decreases, as introduced by Sandborn [26] in the context of boundary layer flows. For a historical overview we refer to [15]. Different definitions of intermittency, for example, a steepening of the energy spectrum proposed by Kolmogorov 1962 [27], can be found, e.g., in Ref. [28].

Related work to quantify the anisotropy of the flow and its intermittency using structure functions of either tensorial components or applying the SO3 decompositions, the latter is based on spherical harmonics, have been proposed in Refs. [29–31]. As structure functions can be linked to wavelet decompositions (see, e.g., [15]), the increments can be seen as wavelet coefficients using the poor man's wavelet (i.e., the difference of two δ distributions), the exponent of the detectable scaling laws is limited by the order of the structure function, and the scale selectivity is reduced because the frequency localization of the poor man's wavelet is rather bad.

A. Orthogonal wavelet decomposition

The starting point is the velocity field $\boldsymbol{u} = (u^{(1)},u^{(2)},u^{(3)})$, sampled at resolution $n = 2^{3J}$, which is decomposed into a series:

$$\boldsymbol{u}(\boldsymbol{x}) = \sum_{j=0}^{J-1}\sum_{\mu=1}^{7}\sum_{i_1,i_2,i_3=0}^{2^j-1} \widetilde{\boldsymbol{u}}_{j,\mu,\boldsymbol{i}}\psi_{j,\mu,\boldsymbol{i}}(\boldsymbol{x}), \tag{6}$$

using 3D orthogonal wavelets $\psi_{j,\mu,\boldsymbol{i}}(\boldsymbol{x})$. The basis functions are constructed by tensor products of one-dimensional wavelets and a periodization technique [32]. The indices are the scale index j (varying from 0 to $J-1$), the spatial index $\boldsymbol{i} = (i_1,i_2,i_3)$ having 2^{3j} values for each j and μ, and the direction index $\mu = 1,\ldots,7$. The directions $\mu = 1,2,3$ correspond to the Cartesian directions, and $\mu = 4,5,6,7$ to additional directions. The wavelet coefficients measure the fluctuations of $\boldsymbol{u}$ at scale 2^{-j} and around position $2^{-j}\boldsymbol{i}$ for each of the seven possible directions μ. Due to orthogonality with respect to j, $\boldsymbol{i}$, and μ, the coefficients are provided by $\widetilde{\boldsymbol{u}}_{j,\mu,\boldsymbol{i}} = \langle \boldsymbol{u},\psi_{j,\mu,\boldsymbol{i}}\rangle$, where $\langle\cdot,\cdot\rangle$ denotes the L^2-inner product. Here, we use Coiflet 12 wavelets having four vanishing moments. The wavelets are well localized in space around position $2^{-j}\boldsymbol{i}$ and scale 2^{-j}, oscillating, and smooth. The scale 2^{-j} is related to the wave number k_j as

$$k_j = k_\psi 2^j, \tag{7}$$

where $k_\psi = \int_0^\infty k|\hat{\psi}(k)|dk / \int_0^\infty |\hat{\psi}(k)|dk$ is the centroid wave number of the chosen wavelet. For the Coiflet 12 used here we have $k_\psi = 0.77$.

The contribution of $\boldsymbol{u}$ at scale 2^{-j} and direction μ can be reconstructed by summation of $\widetilde{\boldsymbol{u}}_{j,\mu,\boldsymbol{i}}\psi_{j,\mu,\boldsymbol{i}}(\boldsymbol{x})$ over all positions $\boldsymbol{i}$:

$$\boldsymbol{u}_{j,\mu}(\boldsymbol{x}) = \sum_{i_1,i_2,i_3=0}^{2^j-1} \widetilde{\boldsymbol{u}}_{j,\mu,\boldsymbol{i}}\psi_{j,\mu,\boldsymbol{i}}(\boldsymbol{x}). \tag{8}$$

The contribution of $\boldsymbol{u}$ at scale 2^{-j} is then obtained by

$$\boldsymbol{u}_j(\boldsymbol{x}) = \sum_{\mu=1}^{7} \boldsymbol{u}_{j,\mu}(\boldsymbol{x}). \tag{9}$$

For more details on wavelets, we refer the reader to pioneering work [13,14] and text books, e.g., Mallat [32]. The influence of the choice of the wavelet on the statistics has been checked and we found that the results are robust given that the wavelet has a sufficient number of vanishing moments; see, e.g., the discussion in Ref. [15].

B. Scale-dependent statistics

1. *Energy spectra, spatial fluctuations, and flatness*

To study the scale-dependent directional statistics component by component $\ell = 1,2,3$, we first define the qth-order moments of the scale-dependent vector $\boldsymbol{s}_j(\boldsymbol{x}) = (s_j^{(1)},s_j^{(2)},s_j^{(3)})$, which is here either the velocity field at scale 2^{-j} and direction μ, $u_{j,\mu}^{(\ell)}$, or the velocity field at scale 2^{-j}, $u_j^{(\ell)}$,

$$M_q\big[s_j^{(\ell)}\big] = \big\langle \big(s_j^{(\ell)}\big)^q \big\rangle, \tag{10}$$

noting that by construction the mean value satisfies $\langle s_j^{(\ell)}\rangle = 0$. The relation between these scale-dependent moments and the qth-order structure functions is given in Ref. [15]. Here, we consider the second-order moment $M_2[s_j^{(\ell)}]$, which is a scale-dependent mean intensity of $s_j^{(\ell)}$, and the fourth-order moment $M_4[s_j^{(\ell)}]$. These moments are related to the scale-dependent spatial fluctuations and the flatness factor.

A preferred direction can be defined as we consider low magnetic Reynolds number turbulence, which is statistically symmetric with respect to the x_3 axis. For the perpendicular components, $\ell = 1,2$, we take the average of these two components, $M_q[s_j^\perp] = \{M_q[s_j^{(1)}] + M_q[s_j^{(2)}]\}/2$. The superscript $\perp$ represents the perpendicular contribution. We hereafter denote $s_j^{(3)}$ by $s_j^\parallel$, which is the parallel contribution.

Using $M_2[s_j^{(\ell)}]$ and Eq. (7), we obtain the wavelet energy spectrum for $s_j^{(\ell)}$, which is defined by

$$E\big[s_j^{(\ell)}\big] = \frac{1}{2\Delta k_j} M_2\big[s_j^{(\ell)}\big], \tag{11}$$

where $\Delta k_j = (k_{j+1} - k_j)\ln 2$ [14,33]. The wavelet spectrum $E[s_j^{(\ell)}]$ corresponds to a smoothed version of the Fourier energy spectrum [13,14]. Thanks to the orthogonality of the

wavelets with respect to scale and direction, we obtain the total kinetic energy $E = \sum_{\ell,j} E[u_j^{(\ell)}] = \sum_{\ell,j,\mu} E[u_{j,\mu}^{(\ell)}]$.

The spatial variability of the energy spectrum at a given wave number k_j can be quantified by its standard deviation:

$$\sigma\left[s_j^{(\ell)}\right] = \frac{1}{2\Delta k_j}\sqrt{M_4\left[s_j^{(\ell)}\right] - \left\{M_2\left[s_j^{(\ell)}\right]\right\}^2}. \tag{12}$$

The scale-dependent flatness factor, which quantifies flow intermittency at scale 2^{-j}, is defined by

$$F\left[s_j^{(\ell)}\right] = \frac{M_4\left[s_j^{(\ell)}\right]}{\left\{M_2\left[s_j^{(\ell)}\right]\right\}^2}. \tag{13}$$

In Ref. [12] it was shown that the flatness is related to the energy spectrum (11) and the standard deviation (12) by

$$F\left[s_j^{(\ell)}\right] = \left(\frac{\sigma\left[s_j^{(\ell)}\right]}{E\left[s_j^{(\ell)}\right]}\right)^2 + 1. \tag{14}$$

2. Scale-dependent anisotropy measures

We introduce measures to quantify scale-dependent spatial flow anisotropy and anisotropic flow intermittency. The anisotropy measure of its scale-dependent mean energy $E[s_j^{(\ell)}]$ can be defined, corresponding to the anisotropy measure based on the Fourier representation of the flow. The anisotropy measure of its spatial fluctuations $\sigma[s_j^{(\ell)}]$ is introduced in analogy with that of $E[s_j^{(\ell)}]$. Then, using Eq. (14), we will find that these quantities provide measures of various types of anisotropic flow intermittency. Here, we consider both component-wise anisotropy and directional anisotropy of the flow.

Component-wise anisotropy. Scale-dependent component-wise anisotropy of energy and its fluctuation at scale 2^{-j} is defined, respectively, by

$$c_E(k_j) = \frac{E[u_j^{\perp}]}{E[u_j^{\parallel}]}, \tag{15}$$

$$c_\sigma(k_j) = \frac{\sigma[u_j^{\perp}]}{\sigma[u_j^{\parallel}]}. \tag{16}$$

The measure of the scale-dependent mean energy, $c_E(k_j)$, corresponds to a smoothed version of the Fourier representation of $c(k)$ in Eq. (5). The measure $c_\sigma(k_j)$ yields the degree of the component-wise anisotropy of the spatial fluctuations. These measures have an exact relation with the component-wise flatness factors of $u_j^{(\ell)}$, i.e., $F[u_j^{\perp}]$ and $F[u_j^{\parallel}]$. Using Eqs. (14)–(16), we get

$$\Lambda_j^C \equiv \left\{\frac{c_\sigma(k_j)}{c_E(k_j)}\right\}^2 = \frac{F[u_j^{\perp}] - 1}{F[u_j^{\parallel}] - 1}. \tag{17}$$

This can be regarded as a scale-dependent measure of component-wise anisotropic intermittency.

Directional anisotropy. Next, representative measures of directional anisotropy at scale 2^{-j} are introduced. These measures are defined as

$$d_E^L(k_j) = \frac{E[u_{j,L}^{\perp}]}{E[u_{j,L}^{\parallel}]}, \tag{18}$$

$$d_\sigma^L(k_j) = \frac{\sigma[u_{j,L}^{\perp}]}{\sigma[u_{j,L}^{\parallel}]}, \tag{19}$$

$$d_E^T(k_j) = \frac{E[u_{j,3}^{\perp}]}{E[u_{j,T}^{\perp}]}, \tag{20}$$

$$d_\sigma^T(k_j) = \frac{\sigma[u_{j,3}^{\perp}]}{\sigma[u_{j,T}^{\perp}]}, \tag{21}$$

where L represents the *longitudinal* direction, i.e., $L = \mu = \ell$. The subscript $\mu = 3$ denotes a *transverse* direction of the perpendicular components, while T corresponds to another *transverse* direction of the perpendicular components, i.e., $T = \mu = 1$ for $u_{j,\mu}^{(2)}$ or $T = \mu = 2$ for $u_{j,\mu}^{(1)}$. For the directional statistics, we consider here only three principal directions, i.e., $\mu = 1$, 2, and 3, of the seven possible directions. The measures $d_E^L(k_j)$ and $d_E^T(k_j)$ correspond to smoothed versions of the Fourier representation $2e^{(3)}(k_3)/\{e^{(1)}(k_1) + e^{(2)}(k_2)\}$ and $\{e^{(1)}(k_3) + e^{(2)}(k_3)\}/\{e^{(1)}(k_2) + e^{(2)}(k_1)\}$, respectively, if we take into account the interpretation of the directional statistics in Ref. [12]. These are respectively related to the following expressions in physical space: $2D^{(3)}(r\hat{\boldsymbol{l}}_3)/\{D^{(1)}(r\hat{\boldsymbol{l}}_1) + D^{(2)}(r\hat{\boldsymbol{l}}_2)\}$ and $\{D^{(1)}(r\hat{\boldsymbol{l}}_3) + D^{(2)}(r\hat{\boldsymbol{l}}_3)\}/\{D^{(1)}(r\hat{\boldsymbol{l}}_2) + D^{(2)}(r\hat{\boldsymbol{l}}_1)\}$. Here $D^{(\ell)}(\boldsymbol{r}) = \langle\{v^{(\ell)}(\boldsymbol{x} + \boldsymbol{r}) - v^{(\ell)}(\boldsymbol{x})\}^2\rangle$, and $v^{(\ell)}$ consists of contributions of $u^{(\ell)}$ to scales larger than or equal to a representative scale 2^{-j}, which are obtained by low-pass filtering using the 3D scaling function at scale 2^{-j}. The unit vector of the x_ℓth Cartesian direction is denoted by $\hat{\boldsymbol{l}}_\ell$.

Using Eqs. (14) and (18)–(21), we obtain the exact relations

$$\Lambda_j^L \equiv \left\{\frac{d_\sigma^L(k_j)}{d_E^L(k_j)}\right\}^2 = \frac{F[u_{j,L}^{\perp}] - 1}{F[u_{j,L}^{\parallel}] - 1}, \tag{22}$$

$$\Lambda_j^T \equiv \left\{\frac{d_\sigma^T(k_j)}{d_E^T(k_j)}\right\}^2 = \frac{F[u_{j,3}^{\perp}] - 1}{F[u_{j,T}^{\perp}] - 1}. \tag{23}$$

These quantify the degree of the scale-dependent anisotropic intermittency in the transverse and longitudinal directions. Intermittency can thus be measured not only in the plane perpendicular or in the direction parallel to the magnetic field $\boldsymbol{B}_0$, but also in the longitudinal or transverse directions. Note that the departure of these measures from unity indicates the degree of flow anisotropy, since these measures are equal to unity for isotropic fields.

IV. NUMERICAL RESULTS

A. Visualization

Visualizing isosurfaces of the modulus of vorticity, $|\boldsymbol{\omega}| =$ const., for different N presented in Fig. 1 yields insight and an intuitive idea on the flow structure. For $N = 0$, where there is no imposed magnetic field, the flow can be regarded as isotropic hydrodynamic turbulence, and it exhibits entangled

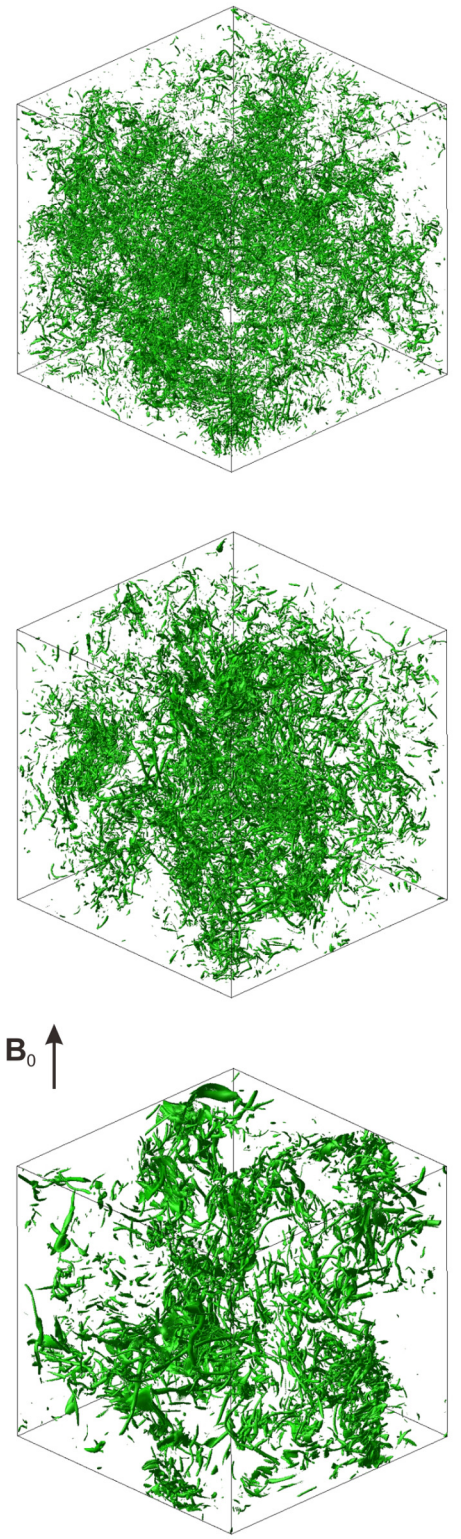

FIG. 1. (Color online) Visualization of intense vorticity regions for $N = 0$ (top), $N = 1$ (middle), and $N = 2$ (bottom) at the final time.

vortex tubes as typically observed in DNS (e.g., [34]) and laboratory experiments (e.g., [35]). In the case of $N \neq 0$, the Lorentz force due to the imposed magnetic field $\boldsymbol{B}_0$, which vanishes for $k_3 = 0$ in wave-number space, gives rise to flow

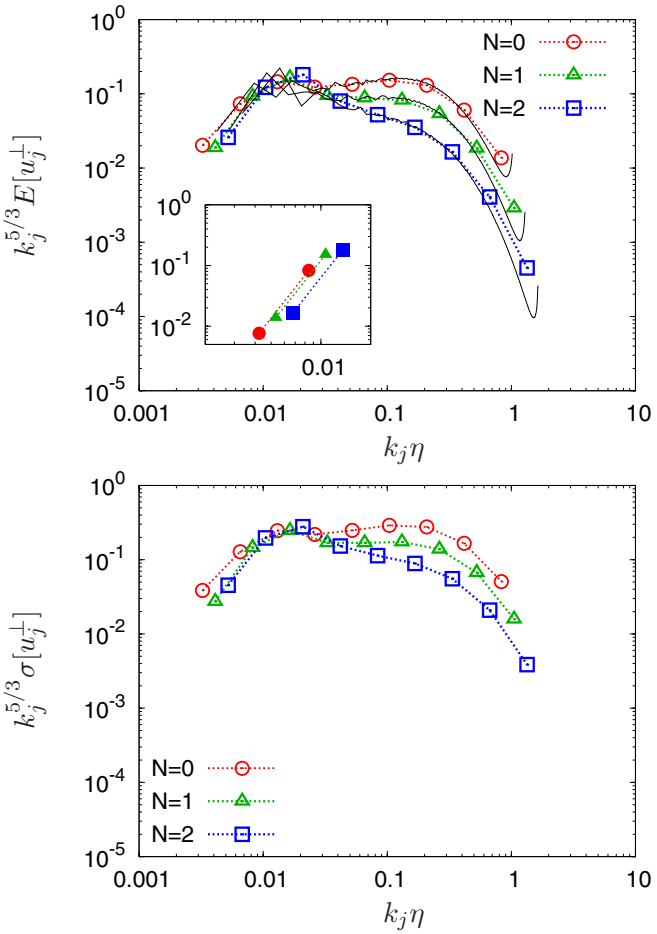

FIG. 2. (Color online) Wavelet mean energy spectra $k_j^{5/3} E[u_j^\perp]$ (top) and standard deviation spectra $k_j^{5/3} \sigma[u_j^\perp]$ (bottom). The Fourier energy spectra are also plotted as reference in the top figure using solid black lines. The three lines with filled circles, triangles, and squares in the inset show the corresponding forcing Fourier spectra $k^{5/3} E_f(k)$.

anisotropy. We see that the structures for relatively weak values of N, e.g., $N = 1$, are similar to those for $N = 0$, as already observed in Ref. [8]. For larger values, e.g., $N = 2$, the structures differ from those observed for $N = 0$ and 1. One may see that many structures are aligned in the direction parallel to $\boldsymbol{B}_0$, an observation consistent with [5]. Thus the visualizations illustrate that the flow at $N = 2$ exhibits a strong anisotropy, which will be quantified statistically in the following.

B. Wavelet mean and standard deviation spectra

The spatial average of the local energy at scale 2^{-j} and its spatial fluctuations are respectively quantified by wavelet mean spectra and standard deviation spectra. Figure 2 (top) shows wavelet mean spectra of the perpendicular component, i.e., $E[u_j^\perp]$ defined by Eq. (11), together with the Fourier energy spectra of the perpendicular component, i.e., $e_\perp(k) = \{e^{(1)}(k) + e^{(2)}(k)\}/2$. All spectra are multiplied by $k^{5/3}$ in order to observe the differences of the spectra at small scales well. We see that the spectra decay with increasing $k_j \eta$, i.e.,

decreasing scale 2^{-j}. Each $E[u_j^\perp]$ (dotted lines in Fig. 2) at a given N is in reasonable agreement with the corresponding Fourier spectrum $e_\perp(k)$ (solid lines in Fig. 2). As N becomes larger, $E[u_j^\perp]$ decays more rapidly for $k_j\eta > 0.1$. This rapid decay of the energy spectra with increasing N is consistent with [6,7]. The inset in Fig. 2 shows the forcing spectra defined by $E_f(k) = \sum_{k-1/2\leqslant|\boldsymbol{q}|\leqslant k+1/2} \widehat{\boldsymbol{u}}(\boldsymbol{q}) \cdot \widehat{\boldsymbol{f}}(\boldsymbol{q})^*/3$, where $*$ denotes the complex conjugate, the factor 3 is due to the component-wise average, and then the right-hand side is real valued for $\widehat{\boldsymbol{f}}(\boldsymbol{k})$ defined by Eq. (3).

Figure 2 (bottom) depicts the standard deviation spectra of $u_j^\perp$, i.e., $\sigma[u_j^\perp]$ defined by Eq. (12). We see that $\sigma[u_j^\perp]$ exhibits more rapid decay in terms of scale with increasing N. Comparing the top and bottom figures shows that the N dependence of $\sigma[u_j^\perp]$ is weaker than that of $E[u_j^\perp]$. The decay of $\sigma[u_j^\perp]$ with increasing N is less pronounced than that of $E[u_j^\perp]$. In Fig. 2, we plotted only the spectra of $u_j^\perp$, but not the spectra of the parallel component $u_j^\parallel$. The latter can be obtained from the anisotropy measures $E[u_j^\perp]/E[u_j^\parallel]$ and $\sigma[u_j^\perp]/\sigma[u_j^\parallel]$, studied below.

C. Scale-dependent component-wise anisotropy

To get a deeper understanding of the scale dependence of anisotropy, we use the scale-dependent anisotropy measures defined by Eqs. (15) and (16). One is $c_E(k_j)$ showing the degree of anisotropy of the wavelet mean energy spectrum at scale 2^{-j}, and the other is $c_\sigma(k_j)$ indicating the degree of anisotropy of the spatial fluctuations of the local energy at scale 2^{-j}. These measures are plotted in Figs. 3 (top) and (bottom), respectively. It is seen that for $N = 0$, which is the isotropic case, $c_E(k_j) \simeq 1$ and $c_\sigma(k_j) \simeq 1$ for $k_j\eta > 0.02$, as expected. The departure from unity indicates the degree of flow anisotropy. In the figures, we focus on their behaviors at small scales, since the forcing is imposed at large scale $k\eta < 0.02$.

Figure 3 (top) shows that for both cases $N = 1$ and 2 the values of $c_E(k_j)$ are smaller than unity, i.e., the scale-dependent energy of the parallel component is predominant over that of the perpendicular component for wave numbers $k_j\eta > 0.05$. These component-wise energies show anisotropy which is persistent at the small scales. The anisotropy becomes more pronounced with increasing N, because $c_E(k_j)$ decreases when N increases. We observe that $c_E(k_j)$ at $N = 1$ is fairly independent of scale for $k_j\eta > 0.05$, and for $N = 2$ it exhibits only weak scale dependence. In the dissipation range, i.e., $k_j\eta > 0.3$, it slightly decays. The scale and N dependences of $c_E(k_j)$ are consistent with previous work which examined $c(k)$ using the Fourier representation [7].

In Fig. 3 (bottom), the values of $c_\sigma(k_j)$ are smaller than unity for both cases, $N = 1$ and 2, and hardly vary with scale. The anisotropy of the spatial fluctuations of the energy is persistent at small scales, as it is the case for the mean value. We see that the N dependence of $c_\sigma(k_j)$ is weaker than that of $c_E(k_j)$. For each N, we also find that $c_E(k_j) < c_\sigma(k_j)$. Thus the anisotropy of the spatial fluctuations of energy is weaker than that of its mean value.

Now, we move on to the scale-by-scale intermittency of the perpendicular velocity components $u_j^\perp$ and the parallel one $u_j^\parallel$. The intermittency can be quantified by the scale-dependent

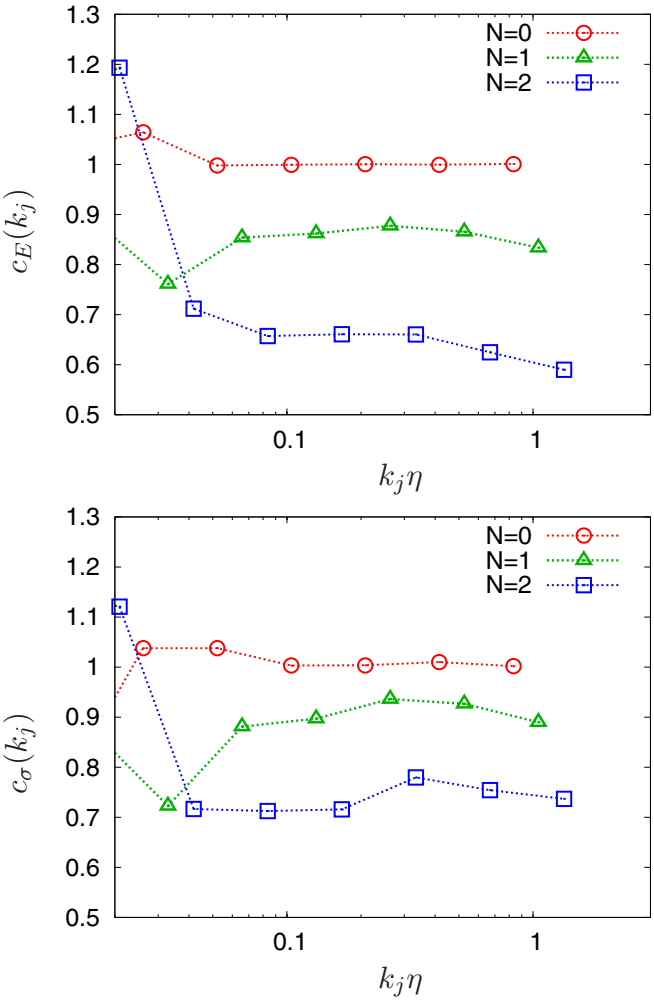

FIG. 3. (Color online) Component-wise anisotropy measures $c_E(k_j)$ and $c_\sigma(k_j)$.

flatness factor defined in Eq. (13). Figure 4 (top) shows that for all N the flatness indeed increases as scale decreases. For small scales $k_j\eta > 0.1$ the flatness also increases as N increases. This shows that the intermittency becomes stronger for increasing N and for decreasing scale. For comparison the inset in Fig. 4 (top) shows the scale-by-scale flatness of the parallel velocity field $F[u_j^\parallel]$. We observe a similar behavior as is the case of $F[u_j^\perp]$.

To quantify the component-wise anisotropy of intermittency at each scale, in Fig. 4 (bottom), we plot the ratio Λ_j^C, which can be equivalently defined by $(F[u_j^\perp] - 1)/(F[u_j^\parallel] - 1)$, that is, $\{c_\sigma(k_j)/c_E(k_j)\}^2$. For $N = 0$ the ratio yields nearly the value one at each scale, as expected from the flow isotropy. For both, $N = 1$ and 2, Λ_j^C is larger than unity for $k_j\eta > 0.1$, i.e., the perpendicular velocity becomes more intermittent than the parallel velocity at the smaller scales. For $k_j\eta > 0.1$ the ratio Λ_j^C increases as N increases and thus the anisotropy of intermittency increases. The ratio at $N = 2$ increases as scale decreases, while the ratio at $N = 1$ only weakly depends on scale. Under the imposed magnetic field, the intermittency shows anisotropy in contrast to the case of mean energy and its standard deviation. As mentioned above, in the case

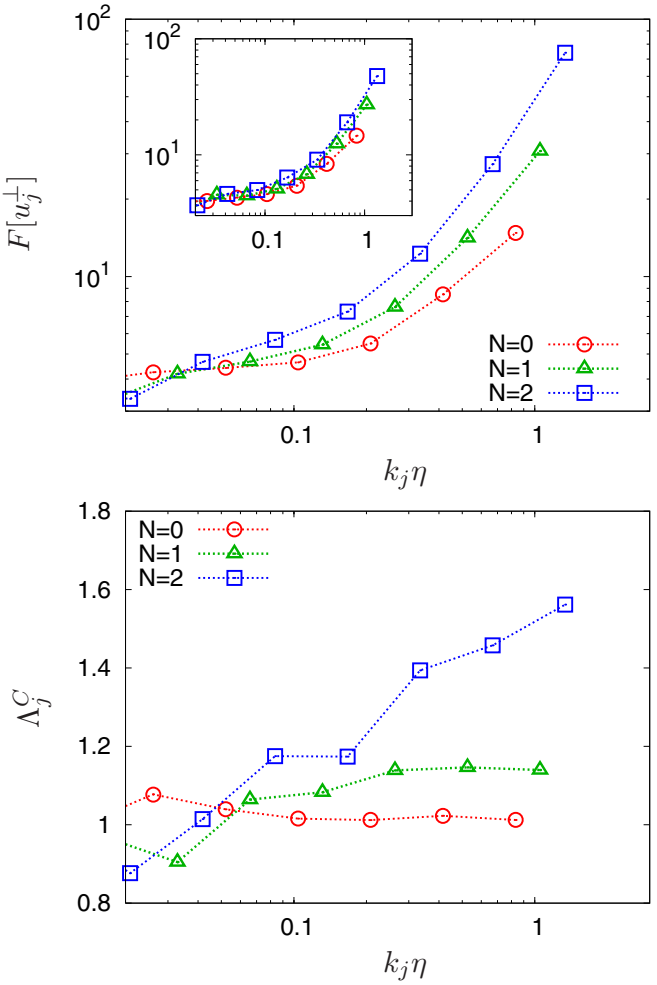

FIG. 4. (Color online) Flatness factor $F[u_j^\perp]$ and the anisotropy measure of intermittency Λ_j^C. The inset shows $F[u_j^\parallel]$.

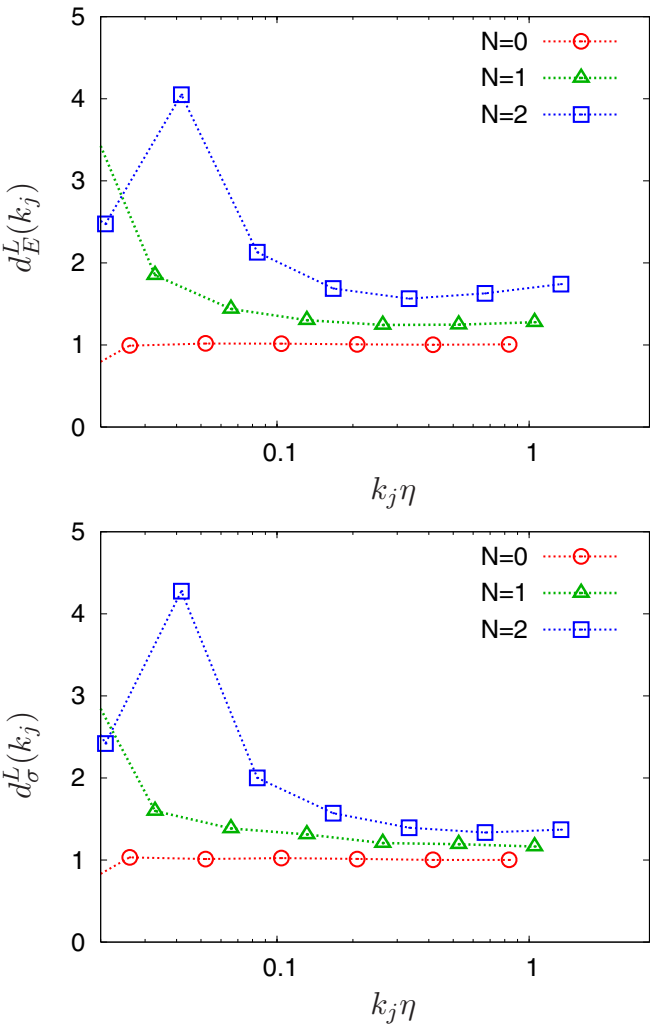

FIG. 5. (Color online) Directional anisotropy measures in the longitudinal direction, $d_E^L(k_j)$ and $d_\sigma^L(k_j)$.

$N \neq 0$, $\{c_\sigma(k_j)/c_E(k_j)\}^2 > 1$ as $c_E(k_j) < c_\sigma(k_j) < 1$. This means that the imposed magnetic field enhances the anisotropy of the mean energy more than of its spatial fluctuations. The component-wise anisotropy of the intermittency thus behaves differently from the anisotropy of the mean energy and its spatial fluctuations.

D. Scale-dependent directional anisotropy

Next, we examine the flow anisotropy in different directions at each scale using the measures of directional anisotropy defined by Eqs. (18)–(21). Figure 5 plots the measures d_E^L and d_σ^L, which show the degree of flow anisotropy in the longitudinal direction for the wavelet mean spectra, and for their spatial fluctuations, respectively. We also see that these measures have values larger than unity for $N \neq 0$, while they remain close to unity for $N = 0$. For $N \neq 0$, the correlation of the velocity component parallel to the imposed magnetic field in its longitudinal direction is suggested to be stronger than the correlation of the perpendicular components in the longitudinal direction. This is consistent with the results obtained by the use of the 1D longitudinal Fourier spectrum for each velocity component [6]. We observe that the scale dependence of the measures becomes weak for $k_j\eta > 0.1$ at nonzero N. The anisotropy of the mean spectra and their spatial fluctuations in the longitudinal direction are almost independent of scale for $k_j\eta > 0.1$, and become stronger as N increases. The N dependence of d_σ^L is weaker than that of d_E^L, as it is the case for the N dependence of anisotropy measures in terms of the flow components c_E and c_σ (see Fig. 3). The scale dependence of d_E^L is different from the scale dependence of anisotropy in the longitudinal direction reported in Ref. [6]. The difference may be attributed to the following: (i) Their Taylor microscale Reynolds number, defined by $R_\lambda\{1 + \langle\epsilon_m\rangle/\langle\epsilon_v\rangle\}^{-1/2}$, is much lower than the R_λ defined in Sec. II, and (ii) their measure is not exactly the same as d_E^L.

Figure 6 (top) and (bottom) presents plots of the $k_j\eta$ dependence of the degrees of anisotropy in the transverse directions for wavelet mean intensities of the perpendicular velocity components $u^\perp$, d_E^T, and for their spatial fluctuations, d_σ^T, respectively. These measures are smaller than unity for $N \neq 0$, which means that the energy in the transversal direction is predominant over that in the $\boldsymbol{B}_0$ direction, while they are almost unity for $N = 0$. The scale dependence and N

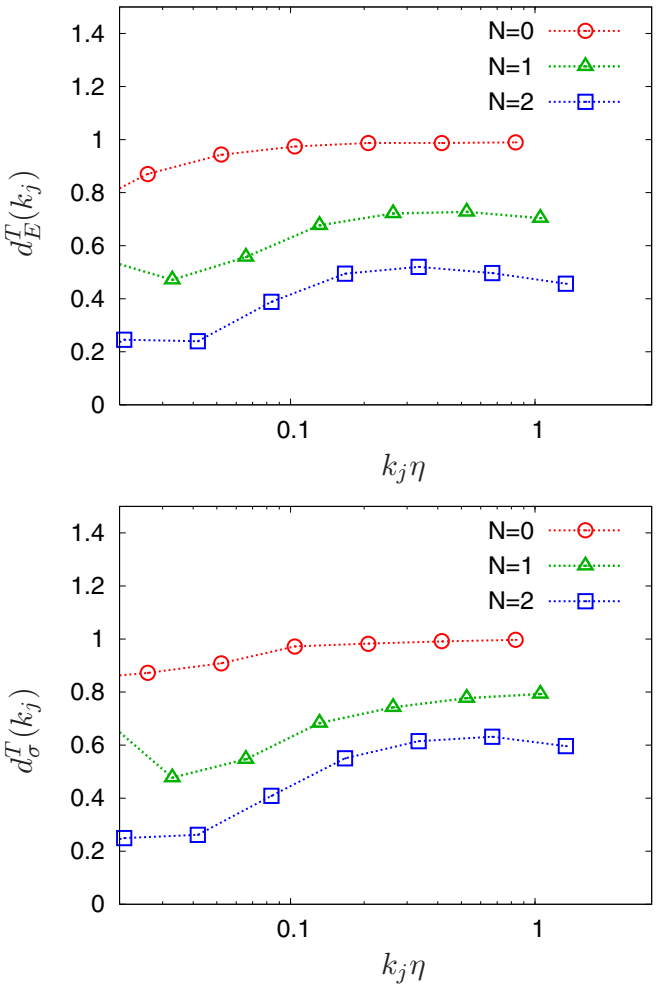

FIG. 6. (Color online) Directional anisotropy measures in the transversal direction, $d_E^T(k_j)$ and $d_\sigma^T(k_j)$.

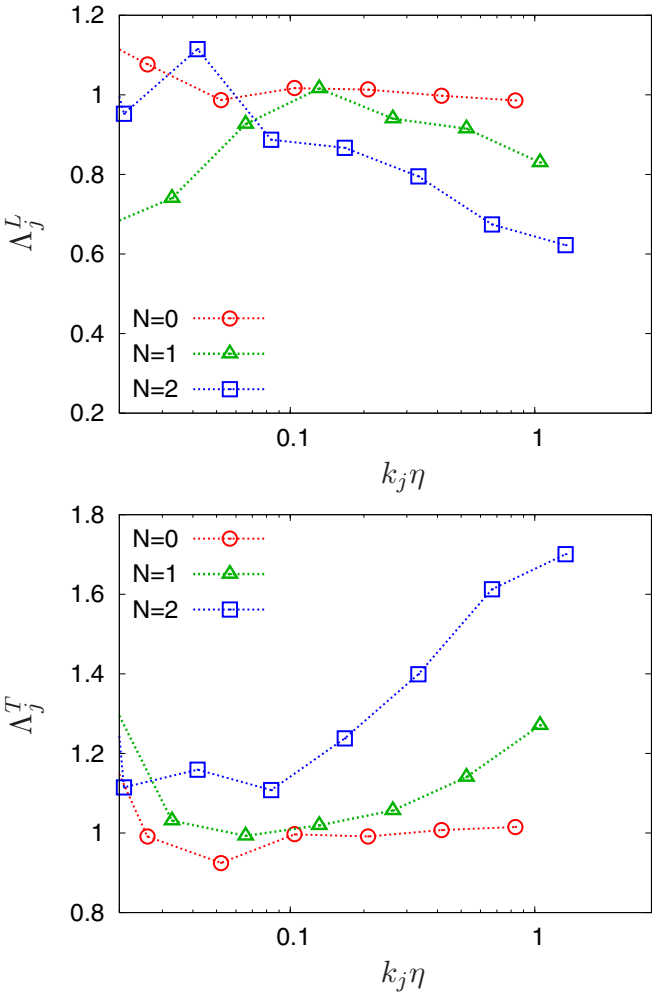

FIG. 7. (Color online) Measures of anisotropic intermittency in the longitudinal direction and the transversal direction, Λ_j^L and Λ_j^T.

dependence of the anisotropy measures in the transverse directions d_E^T and d_σ^T are similar to those of the longitudinal direction d_E^L and d_σ^L. The scale dependence of the measures becomes weak for $k_j\eta > 0.1$ for nonzero values of N. We also observe that the measure d_σ^T is less dependent on N than for d_E^T.

It is suggested that the predominance in d_E^T corresponds to a tendency of alignment of the vorticity structures with $\boldsymbol{B}_0$, which is compatible with the observations in Fig. 1. The turbulent flows are statistically axisymmetric with respect to the direction x_3. Identifying $u^\perp$ and T with $u^{(1)}$ and $T = \mu = 2$, respectively, the quantity d_E^T can be recast into $M_2[u_{j,3}^{(1)}]/M_2[u_{j,2}^{(1)}]$. The inequality $d_E^T < 1$ implies that the contribution of $M_2[u_{j,3}^{(1)}]$ becomes small compared to that of $M_2[u_{j,2}^{(1)}]$. The wavelet energy of $u_j^{(1)}$ is weaker in the direction of $\mu = 3$, i.e., the direction of $\boldsymbol{B}_0$, than in the perpendicular direction $\mu = 2$.

To quantify the scale-dependent anisotropy of intermittency in longitudinal and transversal directions, we use the measures Λ_j^L and Λ_j^T, respectively defined by Eqs. (22) and (23). In Fig. 7, we observe that both measures are scale dependent and differ from unity with decreasing scale. This shows that the anisotropy of intermittency in longitudinal and transversal directions becomes stronger as scale decreases.

V. CONCLUSION AND DISCUSSION

The anisotropy and intermittency of incompressible homogeneous quasistatic MHD turbulence with an imposed magnetic field $\boldsymbol{B}_0$ have been studied. Wavelet-based statistical quantities measuring scale and directional dependence of the flow anisotropy and intermittency have been proposed. Different turbulent MHD flows at moderate Reynolds number, computed by DNS with 512^3 grid points, for three interaction parameters, $N = 0, 1$, and 2 have been analyzed. In the presented work, we focused on directions parallel and perpendicular to $\boldsymbol{B}_0$ and performed flow analysis using orthogonal wavelets, which yield nonredundant flow information in space, scale, and direction. The characterization of the scale-dependent directional intermittency is thus possible, which especially reveals the importance of the external magnetic field driving anisotropy and intermittency along its direction.

Generalizing previously developed wavelet-based measures, introduced by Bos *et al.* [12], we quantified not only the anisotropy of mean values, such as kinetic energy, for different

directions and of different components, but also the anisotropy of its spatial fluctuations. A relation with the anisotropy measured by flatness factors has likewise been established. The anisotropy of fluctuations is shown to be comparable or weaker than that of the mean quantities. The analyses confirmed that the role of the imposed magnetic field $\boldsymbol{B}_0$ is twofold: First, its magnitude plays a significant influence on the flow anisotropy, and second, it is responsible for amplifying the small-scale intermittency. This is in contrast to the case of small-scale intermittency in incompressible rotating turbulence [12] where the Coriolis effect does not enhance small-scale intermittency. Preliminary results were reported in the proceedings [25], where different DNS data considering two values of interaction parameters and a divergence-free random field were analyzed without using the advanced anisotropy measures developed here.

The proposed anisotropy and intermittency measures based on the orthogonal wavelet decomposition can be applied to other quantities, such as vorticity and magnetic fields, and can be used to study anisotropic turbulence encountered in many applications, for example, in geophysical or astrophysical flows. The present results also provide useful information for improving wavelet-based turbulence models for computing anisotropic flows with a reduced computational cost. For a review we refer to [24]. A wavelet-based turbulence model, the coherent vorticity current density simulation (CVCS), which is based on the deterministic computation of the coherent contributions of vorticity and current density using an adaptive wavelet basis, was proposed in Ref. [23]. The coherent field contributions are obtained by filtering out the weak wavelet coefficients, which thus directly exploits the intermittency of turbulence and yields a sparse representation. This approach is motivated from hydrodynamic turbulence for which the coherent vorticity simulation (CVS) has been proposed [36]. We anticipate that CVCS might be more efficient for anisotropic MHD flows thanks to their increased magnetic field driven intermittency.

ACKNOWLEDGMENTS

The computations were carried out on the Earth Simulator and the FX1 system at the Information Technology Center of Nagoya University. This work was supported by Grant-in-Aids for Scientific Research (S) 24224003, (A) 25247014, and (C) 25390149 and by Grant-in-Aid for Young Scientists (B) 24760063 from the Japan Society for the Promotion of Science. M.F. and K.S. thankfully acknowledge financial support from the Association CEA-EURATOM and the FRF2S (French Research Federation for Fusion Studies) for supporting their work within the framework of the EFDA (European Fusion Development Agreement) under Contract V.3258.001. K.S. also acknowledges financial support from ANR, Contract SiCoMHD (ANR-Blanc 2011-045).

[1] P. A. Davidson, *An Introduction to Magnetohydrodynamics* (Cambridge University, Cambridge, England, 2001).
[2] B. Knaepen, S. Kassinos, and D. Carati, J. Fluid Mech. **513**, 199 (2004).
[3] H. K. Moffatt, J. Fluid Mech. **28**, 571 (1967).
[4] U. Schumann, J. Fluid Mech. **74**, 31 (1976).
[5] O. Zikanov and A. Thess, J. Fluid Mech. **358**, 299 (1998).
[6] P. Burattini, M. Kinet, D. Carati, and B. Knaepen, Phys. Fluids **20**, 065110 (2008).
[7] A. Vorobev, O. Zikanov, P. A. Davidson, and B. Knaepen, Phys. Fluids **17**, 125105 (2005).
[8] T. Ishida and Y. Kaneda, Phys. Fluids **19**, 075104 (2007).
[9] D. Montgomery and L. Turner, Phys. Fluids **25**, 345 (1982).
[10] B. Favier, F. S. Godeferd, C. Cambon, and A. Delache, Phys. Fluids **22**, 075104 (2010).
[11] B. Knaepen and R. Moreau, Annu. Rev. Fluid Mech. **40**, 25 (2008).
[12] W. J. T. Bos, L. Liechtenstein, and K. Schneider, Phys. Rev. E **76**, 046310 (2007).
[13] M. Farge, Annu. Rev. Fluid Mech. **24**, 395 (1992).
[14] C. Meneveau, J. Fluid Mech. **232**, 469 (1991).
[15] K. Schneider, M. Farge, and N. Kevlahan, in *Woods Hole Mathematics, Perspectives in Mathematics and Physics*, edited by N. Tongring and R. C. Penner (World Scientific, Singapore, 2004).
[16] K. Yoshimatsu, N. Okamoto, K. Schneider, Y. Kaneda, and M. Farge, Phys. Rev. E **79**, 026303 (2009).
[17] K. Yoshimatsu, K. Schneider, N. Okamoto, Y. Kawahara, and M. Farge, Phys. Plasmas **18**, 092304 (2011).
[18] P. Veltri, Plasma Phys. Control. Fusion **41**, A787 (1999).
[19] R. Bruno, B. Bavassano, E. Pietropaolo, V. Carbone, and P. Veltri, Geophys. Res. Lett. **26**, 3185 (1999).
[20] R. Bruno and V. Carbone, Living Rev. Sol. Phys. **2**, 4 (2005).
[21] M. Farge, G. Pellegrino, and K. Schneider, Phys. Rev. Lett. **87**, 054501 (2001).
[22] K. Yoshimatsu, Y. Kondo, K. Schneider, N. Okamoto, H. Hagiwara, and M. Farge, Phys. Plasmas **16**, 082306 (2009).
[23] K. Yoshimatsu, N. Okamoto, Y. Kawahara, K. Schneider, and M. Farge, Geophys. Astrophys. Fluid Dyn. **107**, 73 (2013).
[24] K. Schneider and O. Vasilyev, Annu. Rev. Fluid Mech. **42**, 473 (2010).
[25] N. Okamoto, K. Yoshimatsu, K. Schneider, and M. Farge, ESAIM Proc. **32**, 95 (2011).
[26] V. A. Sandborn, J. Fluid Mech. **6**, 221 (1959).
[27] A. N. Kolmogorov, J. Fluid Mech. **13**, 82 (1962).
[28] U. Frisch, *Turbulence* (Cambridge University, Cambridge, England, 1995).
[29] S. Kurien and K. R. Sreenivasan, in *New Trends in Turbulence*, edited by M. Lesieur, A. Yaglom, and F. David (EDP Sciences, Les Ulis, France, 2001).
[30] S. Kurien and K. R. Sreenivasan, Phys. Rev. E **62**, 2206 (2000).
[31] L. Sorriso-Valvo, V. Carbone, R. Bruno, and P. Veltri, Europhys. Lett. **75**, 832 (2006).
[32] S. Mallat, *A Wavelet Tour of Signal Processing, Third Edition: The Sparse Way* (Academic, New York, 2010).

[33] P. S. Addison, *The Illustrated Wavelet Transform Handbook: Introductory Theory and Applications in Science, Engineering, Medicine and Finance* (Taylor & Francis, London, 2002).
[34] E. D. Siggia, J. Fluid Mech. **107**, 375 (1982).
[35] S. Douady, Y. Couder, and M. E. Brachet, Phys. Rev. Lett. **67**, 983 (1991).
[36] M. Farge and K. Schneider, Flow, Turbul. Combust. **66**, 393 (2001).